

RESEARCH ARTICLE | OCTOBER 26 2023

State-to-state rovibrational transition rates for CO₂ in the bend mode in collisions with He atoms

Taha Selim ; Ad van der Avoird ; Gerrit C. Groenenboom  



J. Chem. Phys. 159, 164310 (2023)

<https://doi.org/10.1063/5.0174787>



CrossMark

The Journal of Chemical Physics

Special Topic: Algorithms and Software
for Open Quantum System Dynamics

Submit Today

State-to-state rovibrational transition rates for CO₂ in the bend mode in collisions with He atoms

Cite as: J. Chem. Phys. 159, 164310 (2023); doi: 10.1063/5.0174787

Submitted: 2 September 2023 • Accepted: 9 October 2023 •

Published Online: 26 October 2023



Taha Selim,^{a)} Ad van der Avoird,^{b)} and Gerrit C. Groenenboom^{b)}

AFFILIATIONS

Theoretical Chemistry Institute for Molecules and Materials, Radboud University, Heyendaalseweg 135, 6525 AJ Nijmegen, The Netherlands

^{a)}tselim@science.ru.nl

^{b)}Author to whom correspondence should be addressed: gerritg@theochem.ru.nl

ABSTRACT

Modeling environments that are not in local thermal equilibrium, such as protoplanetary disks or planetary atmospheres, with molecular spectroscopic data from space telescopes requires knowledge of the rate coefficients of rovibrationally inelastic molecular collisions. Here, we present such rate coefficients in a temperature range from 10 to 500 K for collisions of CO₂ with He atoms in which CO₂ is (de)excited in the bend mode. They are obtained from numerically exact coupled-channel (CC) calculations as well as from calculations with the less demanding coupled-states approximation (CSA) and the vibrational close-coupling rotational infinite-order sudden (VCC-IOS) method. All of the calculations are based on a newly calculated accurate *ab initio* four-dimensional CO₂-He potential surface including the CO₂ bend (ν_2) mode. We find that the rovibrationally inelastic collision cross sections and rate coefficients from the CSA and VCC-IOS calculations agree to within 50% with the CC results at the rotational state-to-state level, except for the smaller ones and in the low energy resonance region, and to within 20% for the overall vibrational quenching rates except for temperatures below 50 K where resonances provide a substantial contribution. Our CC quenching rates agree with the most recent experimental data within the error bars. We also compared our results with data from Clary *et al.* calculated in the 1980s with the CSA [A. J. Banks and D. C. Clary, J. Chem. Phys. **86**, 802 (1987)] and VCC-IOS [D. C. Clary, J. Chem. Phys. **78**, 4915 (1983)] methods and a simple atom-atom model potential based on *ab initio* Hartree-Fock calculations and found that their cross sections agree fairly well with ours for collision energies above 500 cm⁻¹, but that the inclusion of long range attractive dispersion interactions is crucial to obtain reliable cross sections at lower energies and rate coefficients at lower temperatures.

© 2023 Author(s). All article content, except where otherwise noted, is licensed under a Creative Commons Attribution (CC BY) license (<http://creativecommons.org/licenses/by/4.0/>). <https://doi.org/10.1063/5.0174787>

I. INTRODUCTION

The evolution of interstellar molecular clouds to protostars to protoplanetary disks to planetary systems can be followed by observing spectra emitted or absorbed by small molecules, such as CO, CO₂, HCN, C₂H₂, etc.¹ Microwave spectra are generated by rotational transitions in these molecules, infrared spectra by rovibrational transitions. The shapes of the lines in the spectra depend on the rotational and vibrational level populations, and these populations are determined both by radiative transitions and by transitions caused by molecular collisions with abundant species: hydrogen and helium atoms, H₂ molecules, and electrons. The information from the spectra is used by astronomers in modeling

the processes taking place in the various stages of the evolution. Two situations are distinguished: (1) environments from which the spectra originate are in local thermal equilibrium (LTE) and the line shapes in the spectra only depend on the temperature, and (2) the spectra originate from non-LTE environments. In the first situation it is sufficient to know the Einstein *A* and *B* coefficients for spontaneous and stimulated emission and absorption. In the non-LTE case one also needs to know state-to-state transition rate coefficients from molecular collisions. This paper is concerned with the latter case, and in particular with the calculation of collisional transition rates from first principles. Cross sections and rate coefficients for rotationally inelastic collisions have already been calculated for several astronomically relevant molecular systems including CO₂-He,^{1,2}

but the additional inclusion of vibrational (de)excitations is more demanding. In earlier work^{3–6} we studied rovibrational transitions in CO in collisions with H atoms and rovibrational transitions in the stretch modes of CO₂ in collisions with He atoms.^{7,8} Here, we investigate the bend mode of CO₂ in collisions with He atoms.

Spectra of the CO₂ bend mode in the 15 μm range originating from different astronomical environments were observed by the Infrared Space Observatory (ISO)^{9,10} and the Spitzer Space Telescope¹¹ and, recently, also by the James Webb Space Telescope (JWST).¹² Another process in which collisions of CO₂ in the stretch and bend modes with He atoms are important is the CO₂ laser action.^{13–16} Furthermore, the CO₂ bend mode is relevant because it yields the dominant contribution to the terrestrial greenhouse effect,^{17,18} and collisions with (oxygen) atoms in the mesosphere are important as well.¹⁹ Finally, CO₂ occurs in the atmospheres of other planets and exoplanets²⁰ and its spectra are important in modeling these atmospheres.

The CO₂ molecule has three vibrational modes: a twofold degenerate bend mode with experimental frequency 667 cm^{-1} , a symmetric stretch mode at 1333 cm^{-1} , and an asymmetric stretch mode at 2349 cm^{-1} .²¹ Here, we concentrate on the bend mode. In their pioneering theoretical work on rate coefficients for vibrational transitions in CO₂ induced by collisions with rare gas (Rg) atoms Clary *et al.*^{15,22–26} also investigated the bend mode. In scattering calculations they used the coupled-states approximation (CSA), as well as the VCC-IOS method, a vibrational close-coupling method for the vibrations, combined with the infinite-order sudden (IOS) approximation for the rotations. Although they included the rotational states both in their VCC-IOS calculations¹⁵ and in their CSA calculations,²⁵ they only provided some illustrative data for state-to-state rovibrational transitions. And they used a model potential based on *ab initio* self-consistent field (SCF) calculations, which can nowadays be calculated much more accurately. Experimental data are available only for overall vibrational transition rates.^{27,28} The more advanced models currently being developed by astronomers^{29,30} and the availability of data from JWST require rovibrational state-to-state collisional rate coefficients, which we here present.

Section III describes the *ab initio* calculation of the four-dimensional CO₂–He intermolecular potential depending on the CO₂ bend coordinate. Also the analytical representation of the potential is defined and the potential is illustrated. The bend mode of a linear molecule like CO₂ is twofold degenerate and generates vibrational angular momentum, which makes the theory more complicated than it is for the stretch modes or the bend modes in nonlinear molecules. It is outlined in Sec. IV as part of the CO₂–He scattering approach. In Sec. V we present and discuss our results and compare the overall vibrational transition rates with the available experimental data and with the results of Clary *et al.* Section VI summarizes our conclusions.

II. COORDINATES AND FRAMES

The Jacobi scattering vector points from the center-of-mass of CO₂ to the helium atom. Its Cartesian coordinates with respect to a space-fixed (SF) frame are given by the column vector \mathbf{R} . The spherical polar coordinates of this vector are (R, Θ, Φ) , with $R = |\mathbf{R}|$. In the scattering calculation we express the wave function in a two-angle

embedded body-fixed (BF) frame with the vector \mathbf{R} as its z -axis, which is defined by the rotation matrix $\mathbb{R}(\Phi, \Theta, 0)$. This matrix is written in zyz -Euler angle parameterization using the active rotation convention, see Biedenharn and Louck,³¹ p. 23, i.e.,

$$\mathbf{R} = \mathbb{R}(\Phi, \Theta, 0)\mathbf{R}^{\text{BF}} = \mathbb{R}_z(\Phi)\mathbb{R}_y(\Theta)\mathbf{R}^{\text{BF}}, \quad (1)$$

where $\mathbf{R}^{\text{BF}} = (0, 0, R)^T$ are the BF coordinates of the vector \mathbf{R} . The rotation matrices $\mathbb{R}_z(\Phi)$ and $\mathbb{R}_y(\Theta)$ represent rotations around the z - and y -axes, respectively, see, e.g., Ref. 31 or Eq. (5) in Ref. 32.

We also define a molecule-fixed (MF) frame, which has its z -axis parallel to the vector that connects the two O atoms and which has the bent CO₂ molecule in the xz -plane. The MF coordinates of the Jacobi vector are related to its BF coordinates through

$$\mathbf{R}^{\text{BF}} = \mathbb{R}(\alpha, \beta, \gamma)\mathbf{R}^{\text{MF}}, \quad (2)$$

where $\mathbb{R}(\alpha, \beta, \gamma)$ defines the MF frame with respect to the BF frame $\mathbb{R}^{\text{BF}}(\Phi, \Theta, 0)$. Inverting this equation gives

$$\mathbf{R}^{\text{MF}} = \mathbb{R}(\alpha, \beta, \gamma)^T \mathbf{R}^{\text{BF}} = R \begin{pmatrix} -\sin \beta \cos \gamma \\ \sin \beta \sin \gamma \\ \cos \beta \end{pmatrix}. \quad (3)$$

The superscript T on the rotation matrix means transpose, which gives its inverse, since the matrix is orthonormal. The angle α drops out of the equation because the vector \mathbf{R}^{BF} is invariant under rotations around the BF z -axis. This equation shows that the angles β and γ are related to the spherical polar angles (β', γ') of the vector \mathbf{R}^{MF} by $\beta' = \beta$ and $\gamma' = \pi - \gamma$. In Sec. III we use these angles to define the potential.

Combining Eqs. (1) and (2) we find that the MF frame is given with respect to the SF frame by

$$\mathbb{R}(\Phi, \Theta, 0)\mathbb{R}(\alpha, \beta, \gamma) = \mathbb{R}(\Phi, \Theta, \alpha)\mathbb{R}(0, \beta, \gamma), \quad (4)$$

where on right-hand-side we have a three-angle embedded BF frame $\mathbb{R}(\Phi, \Theta, \alpha)$ and a two-angle embedded MF frame $\mathbb{R}(0, \beta, \gamma)$. We use these frames in the VCC-IOS calculations, see Sec. IV D.

III. FOUR-DIMENSIONAL CO₂(BEND)-He POTENTIAL

The coordinates in the CO₂–He potential $V(\tilde{Q}, R, \beta', \gamma')$ are the spherical polar coordinates (R, β', γ') of the helium atom in the MF frame defined above and the dimensionless amplitude \tilde{Q} of the bend mode in the harmonic approximation, which is defined in Sec. IV A below; the classical turning points are $\tilde{Q} = \pm 1$ for $v = 0$ and $\tilde{Q} = \pm\sqrt{3}$ for $v = 1$.

The potential was calculated with the *ab initio* coupled-cluster method with single and double excitations and perturbative triples, CCSD(T), using the MOLPRO package.³³ The basis was the augmented triple-zeta correlation-consistent polarized (aug-cc-pVTZ) basis of Dunning,³⁴ supplemented with a set of $3s3p2d1f$ midbond functions. These midbond functions were placed on the intersection of the vector \mathbf{R} and an ellipsoid around CO₂, as described in

Refs. 7 and 35. This ellipsoid is chosen such that it corresponds to the midpoint of \mathbf{R} at T-shaped configurations with $\beta' = 90^\circ$ and to the midpoint of the vector connecting He with the nearest O atom in linear configurations with $\beta' = 0^\circ$ and 180° . This choice of the location of midbond functions and the use of geometry dependent exponents prevents overcompleteness of the basis, especially in the short range. In all CCSD(T) calculations the T_1 diagnostic was less than 0.018, which indicates the reliability of the CCSD(T) method. The interaction energies were computed using the Boys and Bernardi³⁶ counterpoise method to correct for the basis set superposition error (BSSE).

In our calculations of the potential surface we kept the C–O bond lengths fixed and used the O–C–O angle as the bend coordinate, whereas in the harmonic approximation used in Sec. IV A below the displacements of the C and O atoms in the CO₂ bend coordinate \tilde{Q} are rectilinear by definition. We tested both alternatives; some results are displayed in Fig. S1 of the supplementary material. They show that the differences are very small, because the bend amplitude remains small. Only at very short distances R where the potential is strongly repulsive, small differences are visible.

The *ab initio* potential was calculated on a grid of 16 000 symmetry-unique points. This grid contained 25 points for R , with step size $0.25 a_0$ for $3.5 \leq R \leq 7 a_0$ and step size $0.5 a_0$ for $7 \leq R \leq 10 a_0$, and four logarithmically spaced points for $10 \leq R \leq 15 a_0$. For β' we used eight Gauss–Legendre quadrature points, ranging from 0 to $\pi/2$ because of symmetry. For γ' we used 16 Gauss–Chebyshev equidistant quadrature points between 0 and π , again because of the symmetry. For the bend coordinate \tilde{Q} we used five points: $\tilde{Q} = 0, 0.5, 1, 1.5, 2$. For a number of near-linear geometries with $\beta' = 8.35^\circ$ and the smallest distance $R = 3.5 a_0$ the He atom is very close to the nearest O atom and the *ab initio* calculations could not be converged. The missing data points were provided by exponentially extrapolating the interaction energies at $R = 4.0$ and $3.75 a_0$. The potential is extremely repulsive in this region and the interaction energies are much higher than the highest collision energy, so these data points do not play a role in the scattering calculations.

The angular dependence of the 4D potential is represented by the expansion

$$V(\tilde{Q}, R, \beta', \gamma') = \sum_{\lambda=0}^{\lambda_{\max}} \sum_{m_\lambda=0}^{\lambda} v_{\lambda m_\lambda}(\tilde{Q}, R) S_{\lambda m_\lambda}(\beta', \gamma') \quad (5)$$

in cosine type tesseral harmonics $S_{\lambda m_\lambda} = [C_{\lambda m_\lambda} + (-1)^{m_\lambda} C_{\lambda - m_\lambda}] / \sqrt{2(1 + \delta_{m_\lambda 0})}$ with $m_\lambda \geq 0$, which are real-valued linear combinations of the Racah-normalized spherical harmonics $C_{\lambda m_\lambda}(\beta', \gamma')$. The potential is symmetric with respect to reflection in the xy -plane, which implies that only terms with even values of $\lambda + m_\lambda$ occur in the expansion.

The expansion coefficients $v_{\lambda m_\lambda}(\tilde{Q}, R)$ were obtained at each grid point (\tilde{Q}_k, R_l) by numerical integration over β' and γ' using Gauss–Legendre and Gauss–Chebyshev quadratures, respectively

$$v_{\lambda m_\lambda}(\tilde{Q}_k, R_l) = \frac{2\lambda + 1}{4\pi} \sum_{i=1}^{16} \sum_{j=1}^{32} w_i w_j' S_{\lambda m_\lambda}(\beta'_i, \gamma'_j) V(\tilde{Q}_k, R_l, \beta'_i, \gamma'_j) \quad (6)$$

with weights w_i and w'_j . The expansion has converged at $\lambda_{\max} = 15$. The expansion coefficients $v_{\lambda m_\lambda}(\tilde{Q}_k, R_l)$ were fitted to a fourth-degree polynomial in \tilde{Q}

$$v_{\lambda m_\lambda}(\tilde{Q}, R_l) = \sum_{p=0}^4 v_{p, \lambda m_\lambda}(R_l) \tilde{Q}^p \quad (7)$$

at each grid point R_l . It follows furthermore that $m_\lambda \leq p$ and since the potential is invariant under overall rotation about the z -axis, that the sum of p and m_λ must be even. Finally, the R -dependence of the coefficients $v_{p, \lambda m_\lambda}(R)$ was represented by the Reproducing Kernel Hilbert space (RKHS) method,^{37,38} which uses two parameters: a smoothness parameter n and a parameter m which ensures that the potential decays as $1/R^{m+1}$ beyond the largest R value in the grid. We chose $n = 2$ and $m = 5$.

In the repulsive short range of the potential at near-linear configurations extremely high peaks occur at some specific geometries. These highly repulsive peaks are not physically important because the system cannot reach these geometries even at high collision energies. However, they cause a problem with the convergence of the spherical expansion. In order to avoid this problem we damped the interaction energies for values larger than $V_0 = 0.1 E_h$ with the smooth damping function

$$V_{\text{damped}}(\tilde{Q}, R, \beta', \gamma') = V_0 + \tanh[\zeta\{V(\tilde{Q}, R, \beta', \gamma') - V_0\}]/\zeta, \quad (8)$$

where $\zeta = 1/V_0$ and $2V_0$ is the maximum value of the damped potential. The range of R values for which the damping is effective depends on the angles β' and γ' . At near-linear structures which β' close to 0 and 180° , damping was applied for $3.5 \leq R \leq 4.75 a_0$ for all γ' . For T-shaped structures the interaction energies are less than V_0 and damping was not needed.

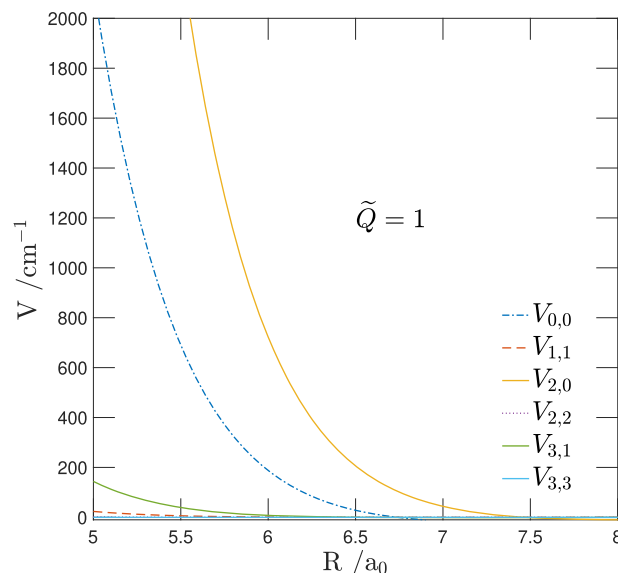


FIG. 1. The first few coefficients in the expansion of the potential in Racah-normalized tesseral harmonics at $\tilde{Q} = 1$.

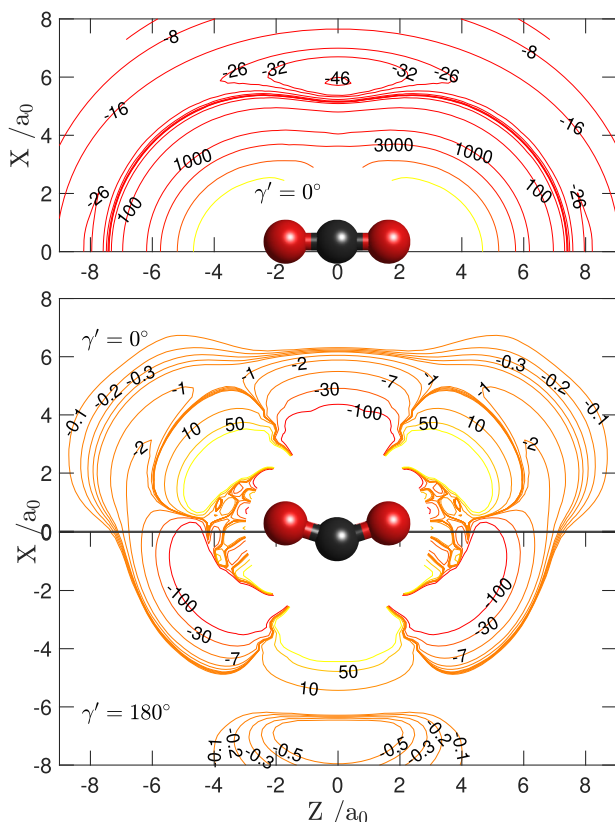


FIG. 2. Contour plots of the $\text{CO}_2\text{-He}$ potential for $\tilde{Q} = 0$ (upper panel) and the difference between the potential for $\tilde{Q} = 1$ and $\tilde{Q} = 0$ (lower panel). The contours in the lower panel are not drawn in the region where the repulsive interaction energy is much higher than the highest collision energy.

The strong anisotropy of the 4D $\text{CO}_2\text{-He}$ potential is obvious already from the large value of $\lambda_{\text{max}} = 15$ needed to converge its spherical expansion. It is further illustrated by showing the first few expansion coefficients $v_{\lambda m_\lambda}(\tilde{Q}, R)$ at $\tilde{Q} = 1$ in Fig. 1. The leading anisotropic term $V_{2,0}$ is larger than the isotropic term $V_{0,0}$, and $V_{3,1}$ is larger than $V_{1,1}$. At the linear configuration with $\tilde{Q} = 0$, only terms with even λ and $m_\lambda = 0$ contribute to the expansion of the potential. Hence, the terms with odd λ and $m_\lambda > 0$ which are due only to the CO_2 bend are smaller. A view of the $\text{CO}_2\text{-He}$ potential for linear CO_2 and the effect of the bending is shown for planar geometries in Fig. 2.

Finally we note that the potential $V(\tilde{Q}, R, \beta', \gamma')$ calculated with coordinates β', γ' relative to the MF frame can simply be expressed relative to the BF frame used in the scattering calculations by the substitution $\beta' = \beta$ and $\gamma' = \pi - \gamma$. This yields an additional factor $(-1)^{m_\lambda}$ in the expansion of the potential in Eq. (5) when applied to the coordinates β and γ .

IV. SCATTERING THEORY

We obtain the cross sections and rate coefficients for rovibrationally inelastic collisions of CO_2 with He by means of scattering

calculations with the numerically exact coupled-channel or close-coupling (CC) method. Since the theory for the bend mode of CO_2 is more complicated than described for the two stretch modes in Refs. 7 and 8, it is outlined below.

A. CO_2 monomer Hamiltonian and wave functions

The bend mode of the CO_2 monomer is twofold degenerate and the molecule bends not only in the xz -plane but also in the yz -plane, with the coordinates (Q_x, Q_y) . The atoms are labeled by the indices $i = 1, 2, 3$ with $i = 1$ and 3 for the two O atoms and $i = 2$ for the C atom. The equilibrium positions in the MF frame are $x_i^e = y_i^e = 0$, $z_1^e = -z_3^e = 2.196 a_0$, and $z_2^e = 0$. We use rectilinear normal coordinates Q_x and Q_y , which involve the atomic displacements Δx_i and Δy_i from their equilibrium positions: $\Delta x_i = c_i Q_x$ and $\Delta y_i = c_i Q_y$. The coefficients c_1 and c_3 are equal, while c_2 is fixed by the condition that the center of mass should not move.

Our CO_2 monomer Hamiltonian is based on Watson's isomorphic Hamiltonian for the bend mode of a linear triatomic molecule.³⁹ In the Cartesian monomer coordinates defined above and with the use of the harmonic-oscillator rigid-rotor approximation it reads

$$\hat{H}_{\text{CO}_2}(Q_x, Q_y) = -\frac{\hbar^2}{2\mu_Q} \left(\frac{\partial^2}{\partial Q_x^2} + \frac{\partial^2}{\partial Q_y^2} \right) + \frac{1}{2} f (Q_x^2 + Q_y^2) + \frac{\hbar^2}{2I_0} (\hat{j}_x^2 + \hat{j}_y^2), \quad (9)$$

where $\mu_Q = 2m_C m_O / (m_C + 2m_O)$ is the reduced mass associated with the bend vibration, m_C and m_O are the masses of the C and O atoms, f is the harmonic force constant, and $I_0 = \sum_{i=1}^3 m_i (z_i^e)^2$ is the rigid rotor moment of inertia for rotation about the x - or y -axis. The harmonic frequency is given by $\omega = \sqrt{f/\mu_Q}$. In the sequel we use dimensionless normal coordinates $\tilde{Q}_x = aQ_x$ and $\tilde{Q}_y = aQ_y$ obtained by scaling with $a = \sqrt{\mu_Q \omega / \hbar}$.

Following textbooks⁴⁰ and previous work²⁵ we may re-express this Hamiltonian in polar coordinates (\tilde{Q}, γ) with $\tilde{Q}_x = \tilde{Q} \cos \gamma$ and $\tilde{Q}_y = \tilde{Q} \sin \gamma$

$$\hat{H}_{\text{CO}_2}(\tilde{Q}, \gamma) = -\frac{\hbar\omega}{2} \left(\frac{\partial^2}{\partial \tilde{Q}^2} + \frac{1}{\tilde{Q}} \frac{\partial}{\partial \tilde{Q}} + \frac{\hat{l}_v^2}{\tilde{Q}^2} \right) + \frac{\hbar\omega}{2} \tilde{Q}^2 + \frac{\hbar^2}{2I_0} (\hat{j}^2 - \hat{j}_z^2), \quad (10)$$

where \tilde{Q} is the bend amplitude and γ is the angle between the plane in which CO_2 bends and the xz plane. The operator $\hat{l}_v = -i \frac{\partial}{\partial \gamma}$ is the dimensionless vibrational angular momentum operator with eigenvalues $l_v = -v, -v+2, \dots, v-2, v$. The eigenvalues of this harmonic-oscillator rigid-rotor Hamiltonian are

$$\varepsilon_{v,l_v,j} = (v+1)\hbar\omega + \frac{\hbar^2}{2I_0} [j(j+1) - l_v^2] \quad (11)$$

and its eigenfunctions, including rotation with respect to the BF frame, are

$$|v, l_v, j, \Omega\rangle = \sqrt{\frac{2j+1}{8\pi^2}} N_{v,l_v} \tilde{Q}^{l_v} \exp(-\tilde{Q}^2/2) L_{(v-l_v)/2}^{l_v}(\tilde{Q}) \times D_{\Omega,l_v}^{(j)}(0, \beta, \gamma)^*, \quad (12)$$

where $D_{\Omega l_v}^{(j)}$ are Wigner D -matrices⁴¹ depending on the rotation angles (β, γ) of the MF frame relative to the BF frame, and Ω is the projection of the monomer angular momentum j on the BF z -axis. Note that in the definition of the polar coordinates (\tilde{Q}, γ) above γ is the angle of the plane in which CO₂ bends and the functions $\exp(i l_v \gamma)$ contained in the basis of Eq. (12) actually belong to the vibrational part. The functions $L_{(v-|l_v|)/2}^{l_v}(\tilde{Q})$ are associated Laguerre functions in the convention of Abramowitz and Stegun⁴² and the normalization constants

$$N_{v,l_v} = \sqrt{2 \frac{\left(\frac{v-|l_v|}{2}\right)!}{\left(\frac{v+|l_v|}{2}\right)!}}. \quad (13)$$

The functions in Eq. (12) may be adapted to the permutation symmetry \hat{P}_{13} that interchanges the two O nuclei, which has the following effect

$$\hat{P}_{13}|v, l_v, j, \Omega\rangle = (-1)^j |v, -l_v, j, \Omega\rangle. \quad (14)$$

A basis adapted to \hat{P}_{13} with parity ϵ reads

$$|v, \tilde{l}_v, j, \Omega, \epsilon\rangle = \frac{1}{\sqrt{2(1+\delta_{l_v,0})}} \left[|v, \tilde{l}_v, j, \Omega\rangle + \epsilon(-1)^j |v, -\tilde{l}_v, j, \Omega\rangle \right], \quad (15)$$

with $\tilde{l}_v = |l_v| \geq 0$. Since ¹⁶O nuclei are bosons with spin $I = 0$ only functions with $\epsilon = 1$ are allowed, which implies that for $l_v = 0$ the basis only contains functions with even j .

B. Coupled-channel calculations

As outlined in earlier papers,^{7,8} our version of the CC method is based on the CO₂-He Hamiltonian in BF coordinates

$$\hat{H} = -\frac{\hbar^2}{2\mu R} \frac{\partial^2}{\partial R^2} R + \hat{H}_{\text{CO}_2}(\tilde{Q}, \gamma) + \frac{\hat{j}^2 + \hat{j}^2 - 2\hat{j} \cdot \hat{j}}{2\mu R^2} + V(\tilde{Q}, R, \beta, \gamma), \quad (16)$$

where $\mu = m_{\text{CO}_2} m_{\text{He}} / (m_{\text{CO}_2} + m_{\text{He}})$ is the reduced mass of the complex, \hat{j} the CO₂ monomer rotational angular momentum operator, \hat{j}^2 the total angular momentum operator of the complex, and $\hat{j}^2 + \hat{j}^2 - 2\hat{j} \cdot \hat{j}$ represents the end-over-end angular momentum operator L^2 in the BF frame.^{43,44} The Hamiltonian \hat{H}_{CO_2} for the CO₂ bend mode is defined in Eq. (10).

The BF channel basis is

$$|v, \tilde{l}_v, j, \Omega, \epsilon; J, M_J\rangle = \sqrt{\frac{2J+1}{4\pi}} |v, \tilde{l}_v, j, \Omega, \epsilon\rangle D_{M_J, \Omega}^{(J)}(\Phi, \Theta, \alpha)^*, \quad (17)$$

where Ω is also the projection of the total angular momentum J on the intermolecular axis R . The permutation symmetry-adapted monomer eigenfunctions $|v, \tilde{l}_v, j, \Omega, \epsilon\rangle$ are defined in Eq. (15). The quantum numbers J and M_J are good quantum numbers, while functions with different Ω are mixed by the Coriolis coupling operator $\hat{j} \cdot \hat{j}$ so that Ω is an approximate quantum number.

Another symmetry is the parity of the complex under overall inversion E^* . The BF channel basis adapted also to inversion is

$$|v, \tilde{l}_v, j, \tilde{\Omega}; \epsilon, P, J, M_J\rangle = \frac{1}{\sqrt{2(1+\delta_{\tilde{\Omega},0})}} \left[|v, \tilde{l}_v, j, \tilde{\Omega}; \epsilon, J, M_J\rangle + P\epsilon(-1)^{\tilde{l}_v+j+J} |v, \tilde{l}_v, j, -\tilde{\Omega}; \epsilon, J, M_J\rangle \right], \quad (18)$$

with $\tilde{\Omega} = |\Omega| \geq 0$ and $P = \pm 1$ being the overall parity. Since P is an exact quantum number the calculations can be made separately for $P = \pm 1$, which is a considerable simplification.

In terms of the symmetry-adapted BF channel basis the scattering wave functions are

$$\Psi^{\epsilon, P, J, M_J} = \frac{1}{R} \sum_{v, \tilde{l}_v, j, \tilde{\Omega}} |v, \tilde{l}_v, j, \tilde{\Omega}; \epsilon, P, J, M_J\rangle \psi_{v, \tilde{l}_v, j, \tilde{\Omega}}^{\epsilon, P, J, M_J}(R). \quad (19)$$

The radial functions $\psi_{v, \tilde{l}_v, j, \tilde{\Omega}}^{\epsilon, P, J, M_J}(R)$ can be obtained in the usual way by solving a set of coupled second order differential equations, the coupled-channel equations. As in Refs. 7 and 8 we do this with the aid of the renormalized Numerov propagator.^{45,46} The required matrix elements of the potential $V(\tilde{Q}, R, \beta, \gamma)$ defined in Sec. III over primitive BF channel basis functions $|v, l_v, j, \Omega; J, M_J\rangle$ are given by

$$\begin{aligned} V_{v' l'_v j' \Omega'; v l_v j \Omega}^{J M_J}(R) &= \delta_{\Omega' \Omega} (-1)^{\Omega - l'_v} \frac{1}{\sqrt{2(1+\delta_{m_\lambda, 0})}} \\ &\times \langle v', l'_v | v_{\lambda m_\lambda}(\tilde{Q}, R) | v, l_v \rangle \begin{pmatrix} j' & \lambda & j \\ -\Omega & 0 & \Omega \end{pmatrix} \\ &\times \left\{ (-1)^{m_\lambda} \begin{pmatrix} j' & \lambda & j \\ -l'_v & m_\lambda & l_v \end{pmatrix} \right. \\ &\left. + \begin{pmatrix} j' & \lambda & j \\ -l'_v & -m_\lambda & l_v \end{pmatrix} \right\}. \end{aligned} \quad (20)$$

The expressions in large round brackets are Wigner $3j$ symbols.⁴¹ With the symmetry-adapted BF basis of Eq. (18) one obtains linear combinations of these matrix elements.

The expansion coefficients $v_{\lambda m_\lambda}(\tilde{Q}, R)$ are defined by Eq. (5) in Sec. III. Their matrix elements over the monomer eigenfunctions $|v, l_v\rangle$ defined in Eq. (12) and containing associated Laguerre functions are calculated by numerical integration over the bend normal coordinate \tilde{Q} with the aid of a five-point Gauss-Laguerre quadrature. Transformation of the matrix elements in Eq. (20) to the symmetry-adapted channel basis in Eq. (18) is easy.

The asymptotic boundary conditions to which we need to match the scattering wave functions at large distance R are defined in terms of a SF channel basis with partial wave quantum numbers L . The monomer wave functions $|v, l_v, j, m_j\rangle$ in the SF frame are the same as those in the BF frame in Eq. (12), except that the Euler angles (α, β, γ) now define the orientation of the MF frame relative to the SF frame and the angular momentum component Ω on the BF z -axis becomes the component m_j on the SF z -axis. The SF monomer basis adapted to \hat{P}_{13} with parity ϵ is

$$|v, \tilde{l}_v, j, m_j; \epsilon\rangle = \frac{1}{\sqrt{2(1+\delta_{l_v,0})}} \left[|v, \tilde{l}_v, j, m_j\rangle + \epsilon(-1)^j |v, -\tilde{l}_v, j, m_j\rangle \right] \quad (21)$$

and the symmetry adapted SF channel basis is

$$|v, \tilde{l}_v, j, L; \epsilon, P, J, M_J\rangle = \sum_{m_j, M_L} |v, \tilde{l}_v, j, m_j; \epsilon\rangle Y_{LM_L}(\Theta, \Phi) \times \langle j m_j L M_L | J M_J \rangle, \quad (22)$$

with $\langle j m_j L M_L | J M_J \rangle$ being a Clebsch–Gordan coefficient⁴¹ and $Y_{LM_L}(\Theta, \Phi)$ a normalized spherical harmonic depending on the polar angles of \mathbf{R} with respect to the SF frame. This basis is also adapted to overall inversion with parity $P = \epsilon(-1)^{\tilde{l}_v + L}$. The primitive BF and SF channel bases are related by the unitary transformation

$$|v, l_v, j, \Omega; J, M_J\rangle = \sum_L |v, l_v, j, L; J M_J\rangle U_{L\Omega}^{JJ} \quad (23)$$

with

$$U_{L\Omega}^{JJ} = \langle j \Omega L 0 | J \Omega \rangle \sqrt{\frac{2L+1}{2J+1}}. \quad (24)$$

The unitary transformation between the parity-adapted BF and SF channel bases then follows from Eqs. (15), (18), and (21). At the end of the propagation of the BF scattering functions to large R we transform them to the SF basis with partial wave quantum numbers L and match them to spherical Bessel asymptotic boundary conditions to obtain the S -matrix. We then compute the state-to-state scattering cross sections $\sigma_{v', \tilde{l}'_v, j' \leftarrow v, \tilde{l}_v, j}(E)$ in the usual way from the S -matrix for a large range of energies E and compute state-to-state rate coefficients with

$$k_{v', \tilde{l}'_v, j' \leftarrow v, \tilde{l}_v, j}(T) = \left(\frac{8k_B T}{\pi \mu} \right)^{1/2} \int_0^\infty \sigma_{v', \tilde{l}'_v, j' \leftarrow v, \tilde{l}_v, j}(E) \left(\frac{E}{k_B T} \right) \times \exp\left(-\frac{E}{k_B T}\right) d\left(\frac{E}{k_B T}\right), \quad (25)$$

where k_B is the Boltzmann constant. The vibrational quenching rate from a rovibrational initial state (v, \tilde{l}_v, j) to a final vibrational state (v', \tilde{l}'_v) is defined as the sum over all final rotational states j' in (v', \tilde{l}'_v)

$$k_{v', \tilde{l}'_v \leftarrow v, \tilde{l}_v, j}(T) = \sum_{j'} k_{v', \tilde{l}'_v, j' \leftarrow v, \tilde{l}_v, j}(T). \quad (26)$$

At thermal equilibrium the total vibrational quenching rate coefficient is computed by Boltzmann averaging over the thermally populated initial states j in the initial vibrational state (v, \tilde{l}_v) with energies $\epsilon_{v, \tilde{l}_v, j}$

$$k_{v', \tilde{l}'_v \leftarrow v, \tilde{l}_v}(T) = \frac{\sum_j (2j+1) \exp(-\epsilon_{v, \tilde{l}_v, j}/k_B T) k_{v', \tilde{l}'_v, j \leftarrow v, \tilde{l}_v, j}(T)}{\sum_j (2j+1) \exp(-\epsilon_{v, \tilde{l}_v, j}/k_B T)}. \quad (27)$$

C. Coupled-states approximation

In the coupled-states approximation (CSA) used in the paper by Banks and Clary²⁵ one neglects the Coriolis coupling terms in

the kinetic energy operator that couple BF basis functions with different Ω . This makes Ω an exact quantum number, so that the CC equations can be separated into subsets of equations for each value of Ω that are much smaller than the full set of CC equations. Moreover, the absolute value of Ω is limited to the smallest of the initial or final j value in the scattering process, which reduces the number of subsets to be included. Altogether, this makes CSA calculations much faster than full CC calculations.

In our version of the CSA method we use the full diagonal part of the BF kinetic energy $[J(J+1) + j(j+1) - 2\Omega^2]/2 \mu R^2$, just as in Ref. 25. As mentioned in Sec. IV B, we use the renormalized Numerov method^{45,46} to obtain the radial scattering wave functions $\psi_{v, \tilde{l}_v, j, \Omega}^{\epsilon, P, J, M_J}(R)$ in Eq. (19). This method propagates the matrices \mathbf{Q}_i defined by

$$\psi(R_{i-1}) = \mathbf{Q}_i \psi(R_i), \quad (28)$$

over a radial grid with points R_i with $i = 1, \dots, n$. The column vectors $\psi(R_i)$ contain the radial functions $\psi_{v, \tilde{l}_v, j, \Omega}^{\epsilon, P, J, M_J}(R_i)$ at grid point R_i . As mentioned in Sec. IV B about the CC method, the BF \mathbf{Q} -matrices at the end of the propagation to large R are transformed to the SF basis with partial wave quantum numbers L with the aid of Eqs. (23) and (24) and matched to the proper asymptotic boundary conditions. In the CSA method we obtain matrices \mathbf{Q}_n^Ω for all Ω values, put them together as diagonal blocks into a large matrix \mathbf{Q}_n over all channels, transform this large \mathbf{Q} -matrix from the BF basis to the SF basis with partial wave quantum numbers L in the same way as in the full CC method, and use the asymptotic boundary conditions to obtain the full S -matrix from which the CSA cross sections are calculated.

D. Rotational infinite-order sudden approximation

We also calculated vibrational and rovibrational (de-)excitation cross sections and rate coefficients for CO₂–He collisions with the VCC-IO approximation. This method was extensively used in the 1980s by Clary and co-workers;^{15,22–25} we briefly outline the theory for collisions with CO₂ in the bend mode.

In the IOS approximation the centrifugal term in the Hamiltonian is replaced by $J(J+1)/2\mu R^2$, so that Ω becomes a good quantum number, and the rotational energy of CO₂ is set to zero.⁴⁷ As a result, the vibrational coupled-channels problem can be solved for fixed orientations of the molecule. Calculations are done for a set of J values ranging from $J = 0$ to $J = J_{\max}$. The vibrational wave functions for CO₂ in the bend mode included in Eq. (12) are

$$|v, l_v\rangle = N_{v, l_v} \tilde{Q}^{|l_v|} \exp(-\tilde{Q}^2/2) L_{(v-|l_v|)/2}^{|l_v|}(\tilde{Q}) \frac{\exp(il_v \gamma)}{\sqrt{2\pi}}, \quad (29)$$

with N_{v, l_v} defined in Eq. (13). When the factor $\exp(il_v \gamma)$ contained in the Wigner matrix $D_{\Omega, l_v}^{(j)}(0, \beta, \gamma)^*$ in Eq. (12) is removed from it, the rotational part of the basis $D_{\Omega, l_v}^{(j)}(0, \beta, 0)^*$ depends only on the angle β , which is the angle between the CO₂ z -axis and the z -axis \mathbf{R} of the BF frame. The interaction potential is symmetric with respect to reflection in the BF xz -plane ($\gamma \rightarrow -\gamma$). Vibrational wave functions that are even or odd for this symmetry can be obtained by writing $\exp(il_v \gamma) = \cos(l_v \gamma) + i \sin(l_v \gamma)$. The normalized cosine

and sine type monomer eigenfunctions are denoted by $|v, \tilde{l}_v, p\rangle$ with $\tilde{l}_v = |l_v|$ and p being even (e) and odd (o), respectively. Only the cosine functions with $p = e$ are needed to calculate vibrational cross sections for transitions involving $v = 0, l_v = 0$.

The vibrational coupled-channel equations are solved for a grid of fixed orientations β_i of the CO₂ monomer z-axis in the BF frame for each value of J . The coupling contains the matrix elements

$$V_{v', \tilde{l}'_v, v, \tilde{l}_v}^{(p)}(R, \beta_i) = \langle v', \tilde{l}'_v, p | V(\tilde{Q}, R, \beta_i, \gamma) | v, \tilde{l}_v, p \rangle \quad (30)$$

over the potential $V(\tilde{Q}, R, \beta, \gamma)$ defined in Sec. III. Integration over the angle γ , which determines the plane in which CO₂ bends, can be done analytically since the potential is expanded in cosine type tesseral harmonics containing $\cos(m_\lambda \gamma)$, see Eq. (5), and the basis contains functions $\cos(\tilde{l}_v \gamma)$ or $\sin(\tilde{l}_v \gamma)$. The \tilde{Q} -dependent part of the basis contains associated Laguerre functions and the integration over \tilde{Q} is done numerically with a Gauss–Laguerre quadrature, as in Sec. IV B.

The VCC problem is solved using the same procedure as outlined for the full CC equations in Sec. IV B. This yields a scattering matrix for each β_i and J with elements $S_{v', \tilde{l}'_v, v, \tilde{l}_v}^{(J, p)}(\beta_i, E)$. The vibrational (de)excitation cross sections can be calculated from these S-matrices by integration over β

$$\sigma_{v', \tilde{l}'_v \leftarrow v, \tilde{l}_v}(E) = \frac{\pi}{2k_v^2} g_v \sum_{J, p} (2J+1) \int_0^\pi \left| S_{v', \tilde{l}'_v, v, \tilde{l}_v}^{(J, p)}(\beta, E) \right|^2 \sin \beta d\beta \quad (31)$$

with $k_v^2 = 2\mu(E - \epsilon_v)$, ϵ_v being the energy of the initial vibrational state v , and g_v a degeneracy factor which depends on \tilde{l}_v of the initial state: $g_v = 1$ for $\tilde{l}_v = 0$ and $g_v = 1/2$ for $\tilde{l}_v > 0$. In our case $g_v = 1/2$ and only $p = e$ contributes. We chose a Gauss–Legendre quadrature grid for the angles β_i , so that the integral over β can be calculated by numerical quadrature.

As explained by Clary in his 1983 paper,¹⁵ VCC-IOS can also be used to compute rovibrational cross sections. The theory in Clary's paper is based on the IOS treatment of atom - symmetric rotor collisions derived by Green.⁴⁸ In this case the rotational states of the molecule are labeled with the quantum numbers j, k and the IOS angle-dependent S-matrix $\bar{S}_{j', k', j, k}^{(J)}(\beta, \gamma, E)$ depends on two angles β and γ . These angles determine the orientation of the molecule in the BF frame and in the IOS scattering calculations they are fixed. In the VCC-IOS method applied to CO₂–He collisions with CO₂ in the bend mode the matrix $S_{v', \tilde{l}'_v, v, \tilde{l}_v}^{(J, p)}(\beta, E)$ in Eq. (31) only depends on the angle β , however. In order to make the connection with the theory in Refs. 15 and 48, we introduce an auxiliary angle χ , which is similar to the extra azimuthal angle χ' defined by Watson in his derivation of the rovibrational Hamiltonian for linear molecules.³⁹ As in the work of Watson, this is a mathematical trick which does not require any additional physical assumptions. The vibrational functions $\Psi_{v, \tilde{l}_v}(\tilde{Q}, \gamma)$ in Eq. (29) are multiplied by a phase factor $\exp(-il_v \chi)$ which gives

$$\Psi_{v, \tilde{l}_v}(\tilde{Q}, \gamma - \chi) = \Psi_{v, \tilde{l}_v}(\tilde{Q}, \gamma) \exp(-il_v \chi) \quad (32)$$

and we compensate for this factor by multiplying the pure rotational wave function $D_{\Omega, l_v}^{(j)}(0, \beta, 0)^*$ in Eq. (12) with $\exp(il_v \chi)$, so we get $D_{\Omega, l_v}^{(j)}(0, \beta, 0)^* \exp(il_v \chi) = D_{\Omega, l_v}^{(j)}(0, \beta, \chi)^*$.

In the VCC part of the calculation, the rotational part of the basis is omitted, the angle β and the auxiliary angle χ are fixed, and the S-matrix $\bar{S}_{v', \tilde{l}'_v, v, \tilde{l}_v}^{(J)}(\beta, \chi, E)$ from the VCC calculations formally becomes a function of two angles, just as in the IOS treatment of atom - symmetric rotor collisions.⁴⁸ The vibrational angular momentum l_v takes the role of the rotational angular momentum projection k in the symmetric rotor. In reality one does not need to vary the angle χ in the IOS calculations because it can be shown that this S-matrix is related to the β -dependent S-matrix in Eq. (31) as

$$\bar{S}_{v', \tilde{l}'_v, \Omega'; v, \tilde{l}_v, \Omega}^{(J)}(\beta, \chi, E) = S_{v', \tilde{l}'_v, v, \tilde{l}_v}^{(J)}(\beta, E) \exp[i(l'_v - l_v)\chi]. \quad (33)$$

This requires the β -dependent VCC S-matrix in the complex basis. The transformation of the VCC S-matrices in the symmetry adapted basis of Eq. (31) to the complex basis is given by Eqs. (14) and (15) in Ref. 15. For $\tilde{l}'_v = 0$ (or $\tilde{l}_v = 0$) it is

$$S_{v', \pm \tilde{l}'_v, v, \pm \tilde{l}_v}^{(J)}(\beta, \chi) = \frac{1}{\sqrt{2}} S_{v', \tilde{l}'_v, v, \tilde{l}_v}^{(J, e)}(\beta, \chi) e^{\pm i(\tilde{l}'_v - \tilde{l}_v)\chi}. \quad (34)$$

Then, following Green⁴⁸ and Clary,¹⁵ we define rotation-vibration S-matrices

$$\bar{S}_{v', \tilde{l}'_v, j', \Omega'; v, \tilde{l}_v, j, \Omega}^{(J)}(E) = \delta_{\Omega', \Omega} \langle l'_v, j', \Omega | \bar{S}_{v', \tilde{l}'_v, v, \tilde{l}_v}^{(J)}(\beta, \chi, E) | l_v, j, \Omega \rangle, \quad (35)$$

containing matrix elements of these two-angle dependent S-matrices over the rotational parts of the CO₂ monomer basis functions

$$|l_v, j, \Omega\rangle = \sqrt{\frac{2j+1}{4\pi}} D_{\Omega, l_v}^{(j)}(0, \beta, \chi)^*. \quad (36)$$

The next step is to transform the S-matrix to a \hat{P}_{13} adapted basis. In general, each element of the S-matrix in the symmetry adapted basis is a linear combination of four unadapted S-matrix elements [see Eq. (12) in Ref. 15], but when the final state has $\tilde{l}'_v = 0$ and the initial state has $\tilde{l}_v > 0$, as in our case, only two terms remain,

$$S_{v', \tilde{l}'_v, j', \Omega'; v, \tilde{l}_v, j, \Omega}^{(J, e)}(E) = \frac{1}{\sqrt{2}} \left[\bar{S}_{v', \tilde{l}'_v, j', \Omega'; v, \tilde{l}_v, j, \Omega}^{(J)}(E) + \epsilon (-1)^j \bar{S}_{v', \tilde{l}'_v, j', \Omega'; v, -\tilde{l}_v, j, \Omega}^{(J)}(E) \right]. \quad (37)$$

Note that our \hat{P}_{13} symmetry label ϵ is a good quantum number, whereas the ϵ in Clary's paper¹⁵ differs from ours by a factor $(-1)^j$ for $l_v \neq 0$. For $l_v = 0$ Clary's ϵ is set to zero.

The rovibrationally inelastic cross sections can be obtained from the S-matrices in Eq. (37)

$$\sigma_{v', \tilde{l}'_v, j', \epsilon \leftarrow v, \tilde{l}_v, j, \epsilon}(E) = \frac{\pi}{k_v^2 (2j+1)} \sum_{j, \Omega} (2J+1) \times \left| S_{v', \tilde{l}'_v, j', \Omega'; v, \tilde{l}_v, j, \Omega}^{(J, e)}(E) \right|^2. \quad (38)$$

The calculation of the matrix elements in Eq. (35) can be carried out analytically when the angle-dependent matrices $\bar{S}_{v',l'_v;v,l_v}^{(J)}(\beta, \chi, E)$ are expanded in spherical harmonics Y_{LM_L}

$$\bar{S}_{v',l'_v;v,l_v}^{(J)}(\beta, \chi, E) = \sqrt{2\pi} \sum_{L,M_L} Y_{L,M_L}(\beta, \chi) S_{v',l'_v;v,l_v}^{(J,L)}(E). \quad (39)$$

The expansion coefficients are given by

$$S_{v',l'_v;v,l_v}^{(J,L)}(E) = \sqrt{2\pi} \int_0^\pi Y_{L,l'_v-l_v}(\beta, 0) S_{v',l'_v;v,l_v}^{(J)}(\beta, E) \sin \beta d\beta. \quad (40)$$

Only $M_L = l'_v - l_v$ contributes, because of the phase factor $\exp[i(l'_v - l_v)\chi]$ in Eq. (33). The $\sqrt{2\pi}$ normalizes the spherical harmonics with the azimuthal angle set to zero. The general expression of the cross sections in terms of the expansion coefficients is rather complex [see Eq. (35) of Green⁴⁸], but again, for our case with $\tilde{l}'_v = 0$ and $\tilde{l}_v > 0$ it is simpler. It corresponds to Eqs. (17)–(20) of Ref. 15 and in our notation reads

$$\sigma_{v',l'_v,j' \leftarrow v,l_v,j}(E) = \frac{\pi}{2k_v^2} \sum_L |\langle L, \tilde{l}'_v - \tilde{l}_v, j, \tilde{l}_v | j' \tilde{l}'_v \rangle|^2 \times \sum_j (2J+1) \left| S_{v',l'_v;v,l_v}^{(J,L,e)} \right|^2, \quad (41)$$

with the expansion coefficients $S_{v',l'_v;v,l_v}^{(J,L,e)}$ for the symmetrized $p = e$ basis obtained from Eq. (40) by writing $S_{v',l'_v;v,l_v}^{(J,e)}(\beta, E)$ instead of $S_{v',l'_v;v,l_v}^{(J)}(\beta, E)$. For our case with $\tilde{l}'_v = 0$ and only even j' the constant B in Eq. (19) of Ref. 15 is 1 for terms with odd values of $j + L$, while it is 0 for even values.

E. Technical details

In this section we specify the parameters used in our scattering calculations. The radial grid in the renormalized Numerov propagator ranges from $R = 3$ to $15 a_0$ in 224 equal steps. We started with an outer R value of $35 a_0$, but found out that this value could be reduced to $15 a_0$ without loss of accuracy in the cross sections. We included bend vibrational states with $v = 0, 1$, and 2 , with $\tilde{l}_v = 0, 1$, and $(0, 2)$, respectively. Convergence tests were carried out in which we also included the $v = 3$ functions with $\tilde{l}_v = (1, 3)$ in the channel basis, but the differences in the cross sections were only about 1% for low collision energies where resonances occur and for the highest energies, and less in the intermediate energy range. So in the final calculations we omitted the $v = 3$ functions. The channel basis contained CO₂ monomer rotational states with a maximum j value of 50 for each v . The minimum j value is \tilde{l}_v .

The cross sections were calculated for collision energies from 1 to 2000 cm⁻¹, with a step size of 0.2 cm⁻¹ for $E \leq 16$ cm⁻¹, 1 cm⁻¹ up to 40 cm⁻¹, 5 cm⁻¹ up to 50 cm⁻¹, 10 cm⁻¹ up to 100 cm⁻¹, and 100 cm⁻¹ up to 2000 cm⁻¹. Sharp peaks occur in the cross sections at low energies, due to resonances, so we had to use a fine energy grid in this region. The maximum value of the total angular momentum J needed to converge the cross sections depends on the energy; it was $J_{\max} = 20$ for $E \leq 100$ cm⁻¹, 35 for $100 < E \leq 500$ cm⁻¹, 50 for $500 < E \leq 1000$ cm⁻¹, 60 for $1000 < E \leq 1500$ cm⁻¹, and 70 for $1500 < E \leq 2000$ cm⁻¹. Not all J values were

actually used; for energies above 16 cm⁻¹ J was increased in steps of 4 and the cross sections were obtained for all J 's by cubic spline interpolation over the available J values. This was allowed because the cross sections summed over both parities vary smoothly with J , except for the resonances at low energies. The integration over energy in Eq. (25) for the rate coefficients was done by first making a cubic spline interpolation of the cross sections at the energies for which they were calculated and next applying the trapezoidal rule on an energy grid with a spacing of 0.2 cm⁻¹. These energies range up to 2000 cm⁻¹, which is sufficient to obtain rate coefficients up to $T = 300$ K. In order to obtain reliable rates up to $T = 500$ K we extrapolated the exponentially decaying high energy tail of the integrand in Eq. (25) by a simple exponential function $a \exp(-bR)$ with coefficients a, b fitted to the integrand at the highest two energies and extended the integration up to an energy of 5000 cm⁻¹.

In the VCC-IOS calculations the integration over β in Eqs. (31) and (40) was done numerically using Gauss–Legendre quadrature. When calculating vibrational (de)excitation cross sections from Eq. (31) we used only 16 fixed monomer angles β_i ranging from 0 to π , but when calculating rovibrationally inelastic cross sections from Eqs. (41) and (40) the number of quadrature points had to be much larger (up to 100) in order to achieve convergence.

Our computer codes were written in the free and open source script language SCILAB, version 6.1.1⁴⁹ and computations were done on a cluster of linux servers.

V. RESULTS AND DISCUSSION

A. Cross sections

Before presenting our results calculated with the potential described in Sec. III, let us mention that we also calculated $v = 1$, $\tilde{l}_v = 1 \rightarrow v' = 0, \tilde{l}'_v = 0$ quenching cross sections with the model potential used by Clary *et al.*,^{15,25} which exponentially depends on the He–O and He–C distances with parameters based on Hartree–Fock calculations. The CSA and VCC-IOS cross sections that we calculated with this potential differ at most by a few percent from the results in Ref. 25, which confirms the correctness of both their and our CSA and VCC-IOS programs. The small differences are probably due to some technical differences between our scattering calculations and those in Ref. 25, which were not specified in all detail.

Figure 3 shows the results of these calculations in comparison with those obtained with the CC, CSA, and VCC-IOS methods and our potential in Sec. III. The results are quite similar for collision energies above 500 cm⁻¹. For the highest energies Clary's potential yields slightly larger cross sections, which is probably due to this potential being more strongly repulsive than ours and the atom-atom model producing a stronger coupling between the $v = 1$ and $v = 0$ bend modes of CO₂. At energies below 500 cm⁻¹ the cross sections from our potential are much larger, with the difference increasing to more than two orders of magnitude at collision energies below 10 cm⁻¹. We note incidentally that in Ref. 25 the lowest energy at which the cross sections were calculated was 0.01 eV, which corresponds to about 80 cm⁻¹. Clary's potential based on SCF calculations completely lacks the attractive dispersion interactions which are present in our potential and we think that this explains the much smaller cross sections that it yields at low collision

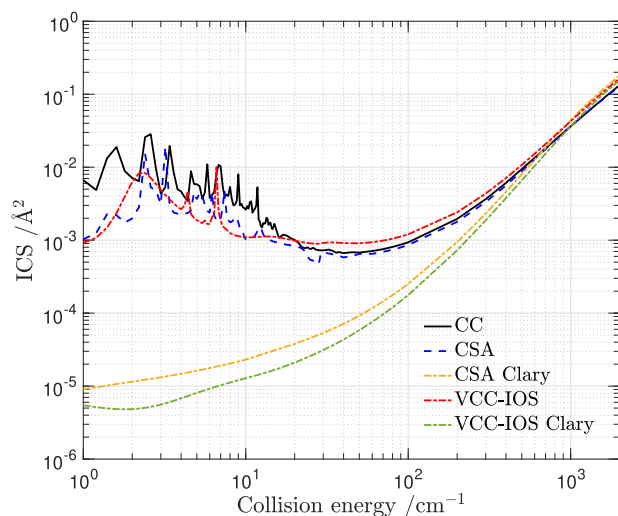


FIG. 3. Vibrational $v = 1, \tilde{l}_v = 1 \rightarrow v' = 0, \tilde{l}'_v = 0$ quenching cross sections from CC, CSA, and VCC-IOs calculations with our potential, in comparison with CSA and VCC-IOs results calculated with the atom-atom model potential of Clary *et al.*^{15,25} In the CC and CSA calculations the initial rotational state has $j = 1$ and the cross sections are summed over all final j' states.

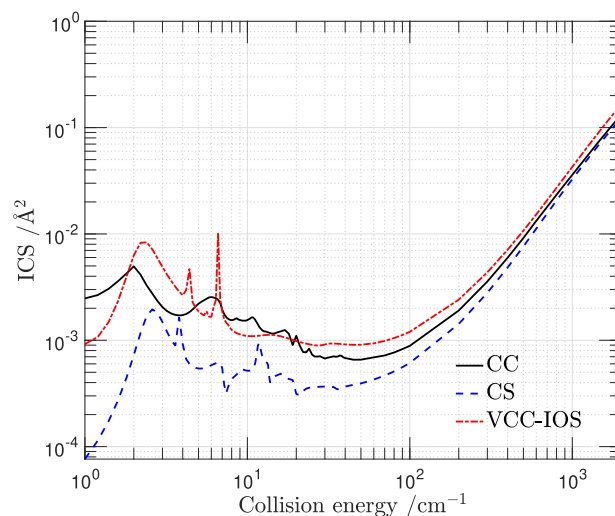


FIG. 4. Vibrational $v = 1, \tilde{l}_v = 1 \rightarrow v' = 0, \tilde{l}'_v = 0$ quenching cross sections from CC, CSA, and VCC-IOs calculations with our potential. In the CC and CSA calculations the initial rotational state has $j = 10$, the VCC-IOs results are the same as in Fig. 3.

energies. Another noticeable difference is the presence of scattering resonances manifested by the peaks in the cross section at energies below 20 cm^{-1} , which are completely missing in the results calculated with Clary's potential. The reason that the latter potential does not produce resonances is that it is purely repulsive, so it has no van der Waals (vdW) minimum, which implies that it cannot give rise to bound or quasi-bound states. Our potential based on presently available computational electronic structure methods is accurate also in the region of the vdW minimum, and the rate coefficients of rovibrationally inelastic collisions presented below can also be trusted at low temperatures.

We see also in Fig. 3 that the total vibrational $v = 1, \tilde{l}_v = 1 \rightarrow v' = 0, \tilde{l}'_v = 0$ quenching cross section obtained from the approximate CSA and VCC-IOs methods agrees fairly well with the result from the numerically exact CC method. Only the subtle resonance structures at low energies are more different, but these depend very sensitively on the potential and on the scattering method used. The CSA and CC cross sections in this figure were computed with the lowest initial $v = 1, \tilde{l}_v = 1$ rotational state with $j = 1$. Figure 4 shows that this holds also for an initial rotational state with $j = 10$, with a resonance structure that is less pronounced. Comparison of Figs. 3 and 4 shows, moreover, that the total vibrational quenching cross section is quite similar for different initial j states.

The CC and CSA methods directly produce rotationally resolved $v = 1, \tilde{l}_v = 1, j \rightarrow v' = 0, \tilde{l}'_v = 0, j'$ cross sections and we explained in Sec. IV D how the VCC-IOs method has been extended¹⁵ to also yield such rotational state-to-state cross sections. The j' product distributions from the different methods are displayed for various collision energies in Figs. 5 and 6 for initial $j = 1$ and $j = 10$, respectively. In Fig. 5 we observe that for initial $j = 1$ higher and higher j' states are excited when the collision energy is increased, which is natural of course, and that the CC, CSA,

and VCC-IOs methods show similar trends. The largest differences occur at the energy of 10 cm^{-1} , but this is in the region where scattering resonances occur. The differences also become larger at higher collision energies, but they typically stay in the range of 20%–50%, with the CSA method yielding smaller j' values than CC and the VCC-IOs method yielding larger j' . In Fig. 6 we observe that for initial $j = 10$ there is a very strong preference for rotationally elastic $j = 10 \rightarrow j' = 10$ transitions, although also here the j' distribution naturally becomes wider at higher collision energies. Again, the different methods produce quite similar results, with the CSA method yielding smaller j' values than CC and the VCC-IOs method yielding larger j' . Also here the largest deviations occur in the region of the resonances at 10 cm^{-1} .

State-to-state $v = 1, \tilde{l}_v = 1, j \rightarrow v' = 0, \tilde{l}'_v = 0, j'$ cross sections from CC, CSA, and VCC-IOs calculations are shown as functions of the collision energy for different j' values in Figs. 7 and 8 for initial $j = 1$ and $j = 10$, respectively. These figures confirm that the cross sections from the approximate CSA and VCC-IOs methods agree to within 50% with those from the full CC method also at the state-to-state level for energies higher than 30 cm^{-1} and that the deviations become larger for lower energies where the resonances occur. Also for larger $\Delta j = |j' - j|$ where the cross sections become smaller the agreement gets somewhat worse. It is striking that the more approximate VCC-IOs method yields cross sections, even at the rotational state-to-state level, that agree as well with the full CC data as the CSA results, and in some cases even better.

Apart from the quality of the approximate CSA and VCC-IOs results in comparison with the full CC data, we may also discuss some general trends in the cross sections. One can observe in the above figures that Δj , the difference between the rotational quantum numbers, is more significant in determining the magnitude of the cross sections than the energy gap between the initial $v = 1$,

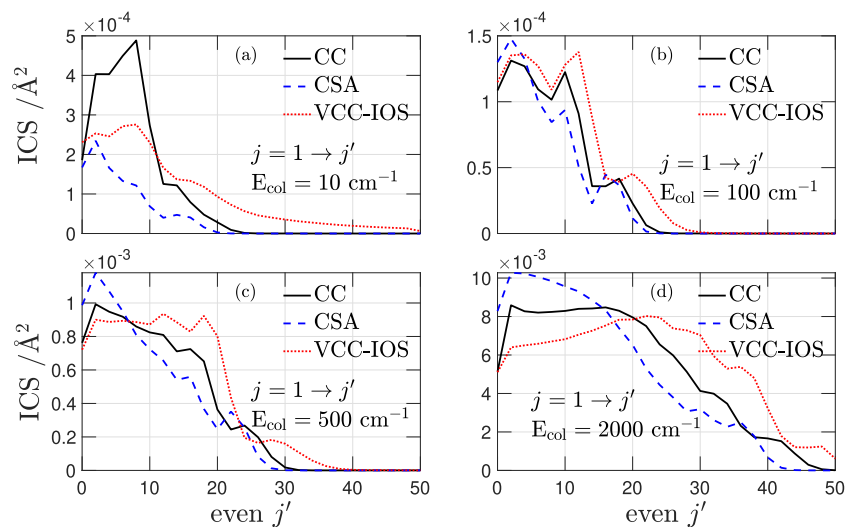


FIG. 5. Product j' distributions in $v = 1, \tilde{l}_v = 1, j \rightarrow v' = 0, \tilde{l}_v' = 0, j'$ transitions with initial $j = 1$ from state-to-state CC, CSA, and VCC-IOS calculations at different collision energies. Panels (a)–(d) correspond to collision energies of 10, 100, 500, and 2000 cm^{-1} , respectively.

$\tilde{l}_v = 1, j$ and final $v' = 0, \tilde{l}_v' = 0, j'$ states. We note here that the energy gap between the lowest vibrationally excited state with $v = 1, \tilde{l}_v = 1, j = 1$ and the $v' = 0, \tilde{l}_v' = 0, j'$ state is smallest for $j' = 41$. Generally the cross sections are smallest in the energy range between 30 and 100 cm^{-1} and increase by at least two orders of magnitude when the energy is raised to 2000 cm^{-1} . This increase is larger when Δj is larger.

A feature in Figs. 7 and 8 that is particularly striking is that the cross sections from CSA calculations become very small for collision energies below 2 cm^{-1} . This may be explained as follows. In the BF coordinates on which the CSA method is based the centrifugal

barrier is represented by a term that includes diagonal and off-diagonal Coriolis couplings, see Eq. (16). The latter are omitted in CSA, which effectively increases the height of the centrifugal barrier. This implies that at low energies the colliding CO_2 molecule and He atom are more strongly prevented from getting closer, where the potential coupling is larger and the vibrational transitions occur. We confirmed this explanation by CSA calculations in which we lowered the centrifugal barrier by adding a term to the diagonal angular kinetic energy that more or less compensates for the omission of the off-diagonal terms. Indeed, we found that this brings the CSA cross sections at low energies substantially closer to the CC results. In Fig. 8(a)

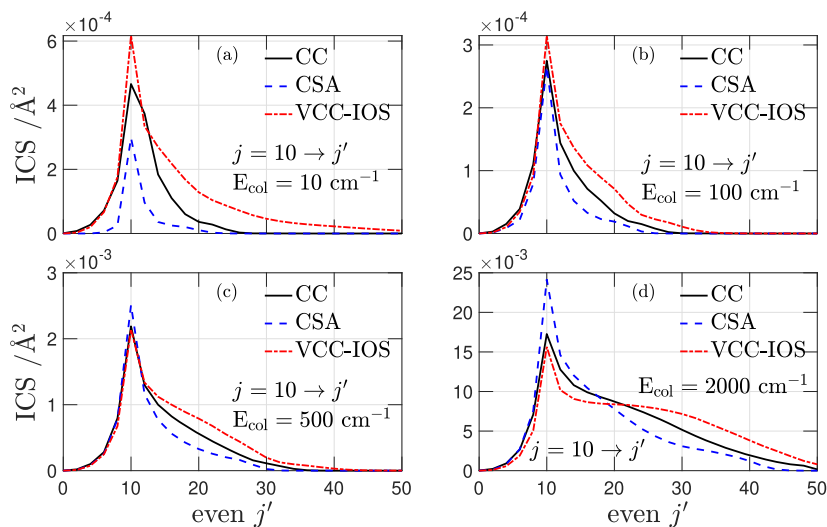


FIG. 6. Same as Fig. 5, with initial rotational state $j = 10$. Panels (a)–(d) correspond to collision energies of 10, 100, 500, and 2000 cm^{-1} , respectively.

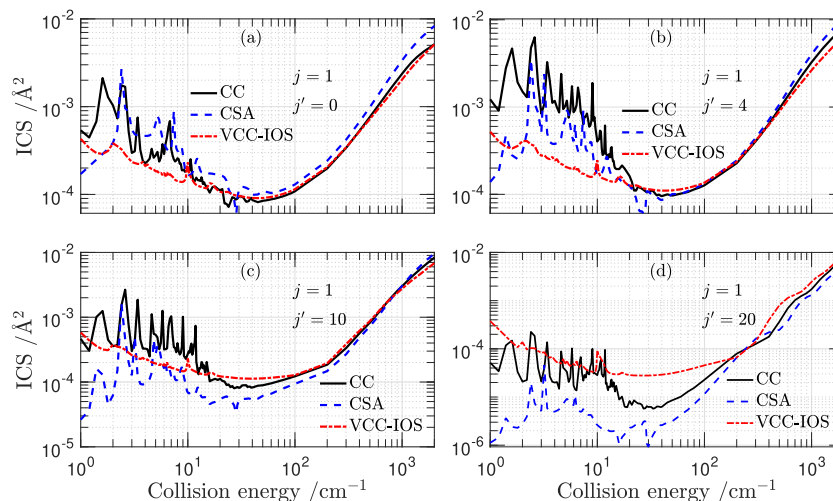


FIG. 7. State-to-state cross sections as functions of the energy for $v = 1, \bar{l}_v = 1, j \rightarrow v' = 0, \bar{l}_v' = 0, j'$ transitions with initial $j = 1$ and different j' from state-to-state CC, CSA, and VCC-IOs calculations. Panels (a)–(d) correspond to $v' = 0$ final states with $j' = 0, 4, 10$, and 20 , respectively.

the CSA cross sections are smaller than those from CC even at higher energies, but also the CC cross sections are extremely small in that case.

Another interesting observation regards the partial cross sections from different total angular momenta J and different parities. Instead of the total parity P with respect to overall inversion, we consider the spectroscopic parity $P(-1)^J$. States with even and odd spectroscopic parity are conventionally labeled e and f , respectively. The partial cross sections for different J values summed over both parities are displayed in Fig. S2. One observes, quite naturally, that for higher collision energies the contributions from higher J 's become more important. And that the maximum values of $J = 20, 50$, and 70 used in different energy ranges produce well converged

cross sections. Since the initial monomer angular momentum is $j = 1$ in this example, the total angular momentum J is nearly equal to the orbital angular momentum L , see Sec. IV B, which is related to the impact parameter b as $L = \mu bv$. From the data shown in Fig. S2 it follows then that the impact parameters are $b = 3.24, 2.05$, and $2.08 a_0$ for collision energies of $100, 1000$, and 2000 cm^{-1} . These impact parameters are small, especially at higher energies, which indicates that (ro)vibrational transitions mostly take place for nearly head-on collisions and happen in the region where the potential is strongly repulsive and the coupling potential is relatively large, see Fig. 2.

The relative contributions from the scattering states with spectroscopic parities e and f to the total cross sections are less obvious,

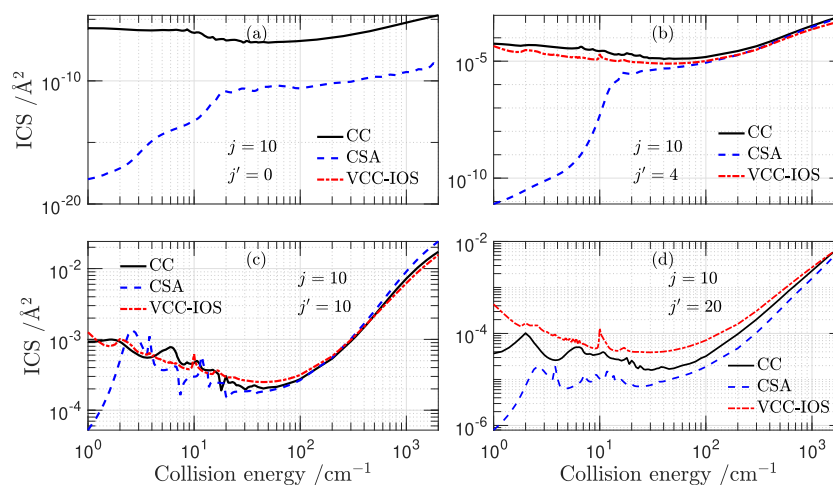


FIG. 8. Same as Fig. 7, with initial rotation state $j = 10$. Panels (a)–(d) correspond to $v' = 0$ final states with $j' = 0, 4, 10$, and 20 , respectively.

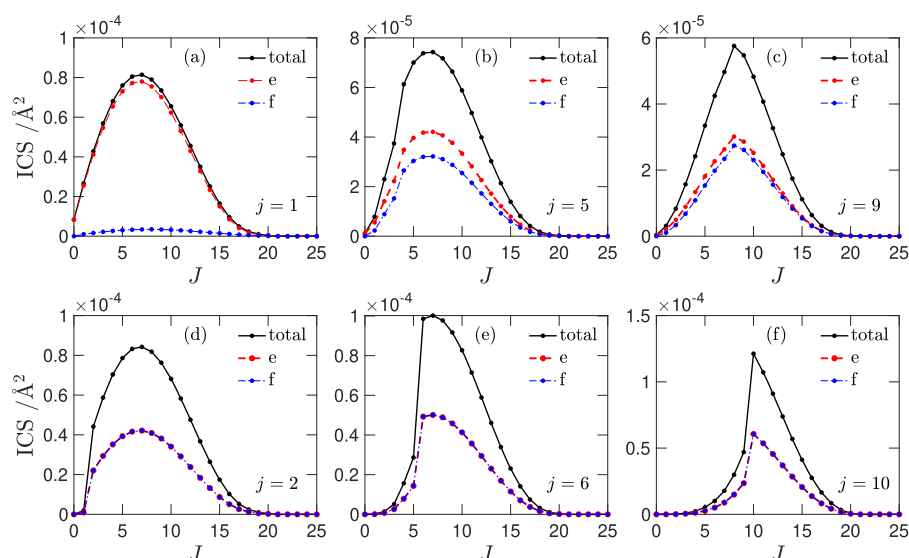


FIG. 9. Partial wave distributions of the $v = 1, \tilde{l}_v = 1, j \rightarrow v' = 0, \tilde{l}'_v = 0$ cross sections computed at the CC level at collision energy $E = 100 \text{ cm}^{-1}$ summed over all final j' values and resolved by spectroscopic parity e or f . Panels (a)–(c) correspond to the odd initial j values 1, 5, and 9, panels (d)–(f) to the even j values 2, 6, and 10. The closed black curves are the total partial cross sections, the dashed red and dot-dashed blue curves are the contributions from parities e and f , respectively. Note that for odd initial j the contributions from parity e are dominant, especially for $j = 1$, while for even j the contributions from parities e and f are nearly equal.

see Fig. 9. For initial $j = 1$ the contributions from the e states are very dominant, and also for higher odd j values the e states contribute more to the cross sections than the f states. For even initial j values, on the other hand, the contributions from the e and f states are practically equal. This can be explained by considering the role of the approximate quantum number Ω in the BF formalism explained in Sec. IV B. The absolute value of Ω is limited by the initial j value, the final j' value, and the total angular momentum J . When analyzing the state-to-state cross sections, we found that the largest allowed absolute Ω values yield the largest contributions. It follows from Eq. (15) that for the ground state with $v' = \tilde{l}'_v = 0$ only states with even j' are allowed, and from Eq. (18) that for $j' = \Omega = 0$ only states with parity e occur. Furthermore, it follows from the second and third $3j$ symbols in Eq. (20) with $l_v = 1$ and $l'_v = 0$ that m_λ must be odd, from the reflection symmetry of the potential in Sec. III that also λ must then be odd, and from the first $3j$ symbol in Eq. (20) that for $\Omega = 0$ the sum of j and j' must be odd as well. We already derived that j' must be even, so only for odd initial j values the $\Omega = 0$ states contribute to the cross sections. Because these $\Omega = 0$ states are purely of parity e , this explains the observed dominance of the e states over the f states in the cross sections with odd initial j . For the initial states with even j the cross sections do not contain this $\Omega = 0$ component with pure e parity and therefore the e and f parity contributions are equal. The dominance of the e states over the f states for odd initial j values is most pronounced for initial $j = 1$ and decreases with increasing j . This follows because for the initial $v = 1, \tilde{l}_v = j = 1$ state $|\Omega|$ is limited to 0 and 1, and the restriction to even j' implies that only the $\Omega = 0$ state with parity e contributes to the cross section through the potential, see Eq. (20). For larger j and j' also $\Omega \neq 0$ states contribute directly to the cross sections through the potential

and the relative contribution from the $\Omega = 0$ states becomes less important.

Another feature that can be observed in Figs. 9(d)–9(f) where the cross sections do not contain the $\Omega = 0$ contribution is that for total J smaller than j and j' , where the maximum $|\Omega|$ is limited by J , the partial cross sections remain small and rise steeply when J becomes equal to the minimum of j and j' . This confirms that, indeed, functions with $|\Omega|$ equal to $\min(j, j')$ yield the largest contributions to the cross sections. Since Ω is the projection of the CO_2 angular momentum j on the intermolecular axis \mathbf{R} this suggests that for rovibrational transitions involving the CO_2 bend mode sideways collisions are most effective. Figure S3 in the supplementary material shows the e/f parity-resolved state-to-state cross sections for initial states with $j = 9$ and $j = 10$ and final j' values ranging up to 25. This figure shows that our findings regarding the different parity contributions to the cross sections for odd and even initial j values also hold for the state-to-state cross sections: the e parity contributions dominate over those of f parity for odd $j = 9$, especially for low final j' , while the e and f contributions are equal for even $j = 10$. It also shows that the j' dependence of the state-to-state cross sections is similar to the total J dependence of the partial cross sections in Fig. 9, which follows from the limitation of the maximum $|\Omega|$ by both j' and J .

B. Rate coefficients

In Fig. 10 we display some state-to-state $v = 1, \tilde{l}_v = 1, j \rightarrow v' = 0, \tilde{l}'_v = 0, j'$ rovibrational transition rates from CC calculations for different initial j and final j' values as functions of the temperature. Such rovibrational state-to-state rates are the data needed in radiative transfer models. For lower initial j the rates of transi-

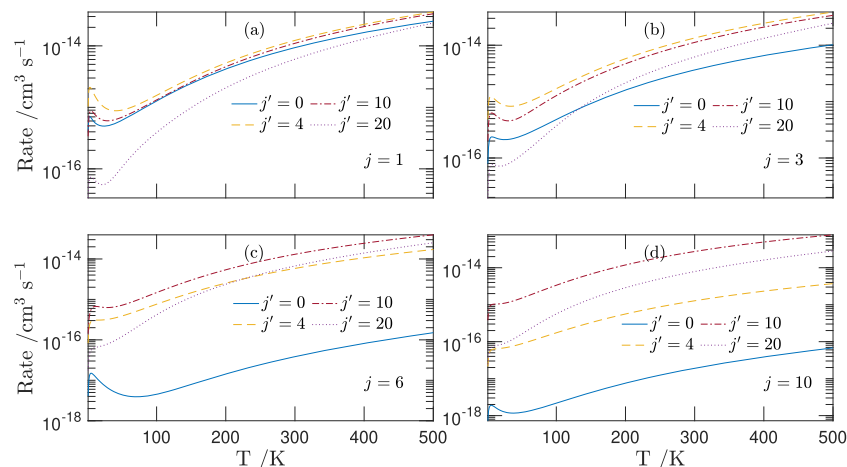


FIG. 10. State-to-state transition rate coefficients from CC calculations for different initial j and final j' values. Panels (a)–(d) correspond to $v = 1$ initial states with $j = 1, 3, 6$, and 10 , respectively.

tions to different j' states differ by at most one order of magnitude at low temperature and become more similar with increasing temperature. For higher initial j one clearly observes that transitions to $j' = j$ are the strongest and that especially transitions to j' smaller than j are weak. More generally, these features indicate that transitions with small $\Delta j = |j' - j|$ are favored and that transitions with $j' > j$ are stronger than those with $j' < j$. The latter propensity can be explained by the energy gap law: the energy difference between the initial $v = 1, j$ and final $v' = 0, j'$ states is smaller when $j' > j$. We will include a more complete set of rovibrational transition rates in the LAMDA data base.⁵⁰

Figures S4 and S5 in the supplementary material show the state-to-state $v = 1, \tilde{l}_v = 1, j \rightarrow v' = 0, \tilde{l}'_v = 0, j'$ rovibrational transition rates for initial $j = 1$ and 10 and different final j' values from CC, CSA, and VCC-IOS calculations. Both the CSA and VCC-IOS rates agree to within about 50% with the CC results, just as the corresponding cross sections, except when j' is smaller than j and the rates become insignificant.

The rates increase monotonically with the temperature, except for transitions involving low j or low j' states for which the rates have minima around 50 K. The relatively large rates at low temperature for these transitions are due to contributions from scattering resonances, as shown in Fig. 7. This figure shows the strongest scattering resonances in the cross sections from CC calculations, weaker ones in the CSA results, and practically none in the VCC-IOS cross sections, which clearly explains why the minima in the rate coefficients from the CC, CSA and VCC-IOS methods in Figs. S6 and S7 of the supplementary material are strongest for CC, weaker for CSA, and absent for VCC-IOS.

In Figs. S6 and S7 of the supplementary material we compare the total vibrational quenching rates, i.e., the rovibrational transition rates summed over all final j' values, calculated with the different methods, with initial $j = 1$ and 10 in the CC and CSA methods. No initial j value is defined in the VCC-IOS method, so the VCC-IOS quenching rates are identical in the two figures. Also the CC and CSA quenching rates are quite similar for $j = 1$ and $j = 10$, except at

the lowest temperatures where the minima are more pronounced for initial $j = 1$, due to the stronger resonance contributions at low j . We observe that the CSA method somewhat underestimates the rates from CC calculations, while the VCC-IOS method yields slightly higher rates. The differences are quite small, however, on the order of 20% or less. These differences between the approximate CSA and VCC-IOS methods and the CC method are smaller than in many of the state-to-state rate coefficients shown in Figs. S4 and S5, which is because the smaller state-to-state rates are more sensitive to the approximations made than the most significant ones. The larger total vibrational quenching rates from VCC-IOS and smaller rates from CSA, as compared to the CC results, are due to the contributions from higher final j' values such as shown in Figs. S4(d) and S5(d). We already concluded from Figs. 5 and 6 that these are favored by VCC-IOS relative to CC and disfavored by CSA.

Figure 11 shows the total vibrational quenching rates for initial j values ranging from 1 to 10. It shows even more clearly that the total vibrational quenching rate hardly depends of the initial j , except at temperatures below 50 K where the rates for low initial j values are enhanced by resonance contributions. This figure also shows that our calculated total vibrational quenching rate agrees with the most recent experimental data within the error bars, which confirms the accuracy of our results.

The rovibrational transition rate coefficients presented in this paper refer to vibrational de-excitation from $v = 1, \tilde{l}_v = 1, j$ to $v' = 0, \tilde{l}'_v = 0, j'$. The corresponding rovibrational excitation rates can be easily obtained from the detailed balance relation.⁵¹ In our previous papers on CO₂-He collisions with CO₂ excited in the stretch modes^{7,8} we also investigated the accuracy of cross sections and rate coefficients from the multi-channel distorted-wave Born approximation (MC-DWBA) and the nearest-neighbor Coriolis coupling (NNCC) method, which is an extension of the CSA method, and we compared the computational efficiency of both methods relative to CC. Our conclusion was that cross sections and rates from the MC-DWBA method are practically equal to those from the full CC method, or from the NNCC method when

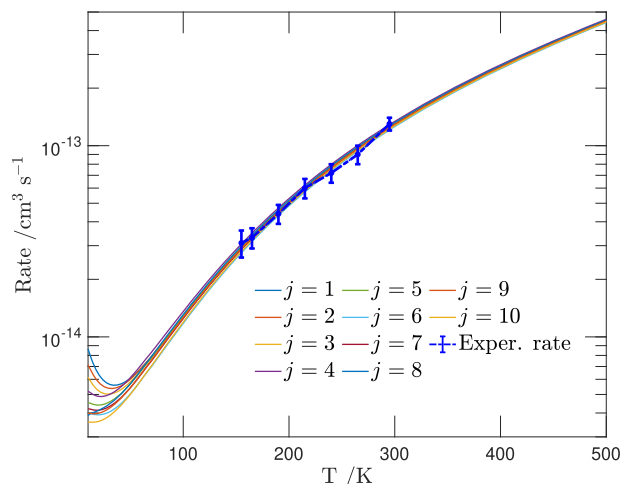


FIG. 11. Vibrational quenching rates from CC calculations for $v = 1, \tilde{l}_v = 1$, $j \rightarrow v' = 0, \tilde{l}_{v'} = 0$ transitions with different initial j values ranging from 1 to 10 compared with experimental results.²⁸

MC-DWBA was combined with the latter method. The extension of CSA to NNCC resulted in better agreement with full CC results. We did not investigate these methods in the present paper on the bend mode of CO₂, but we expect similar results in terms of accuracy and efficiency.

VI. CONCLUSIONS

With the use of a newly computed four-dimensional CO₂–He potential which includes the CO₂ bend coordinate we calculated the cross sections $\sigma_{v',l_v',j' \leftarrow v,l_v,j}(E)$ and rate coefficients $k_{v',l_v',j' \leftarrow v,l_v,j}(T)$ of rovibrational transitions between different bend vibrational and rotational (v, j) states of CO₂ induced by collisions with He atoms. The quantum number l_v represents the vibrational angular momentum generated by the bend mode of CO₂, which is linear at equilibrium. In our scattering calculations we used the numerically exact coupled-channels (CC) method, but also the coupled-states approximation (CSA) and the vibrational close-coupling rotational infinite-order sudden (VCC-IOS) approximation. The effects of each of these approximations on the rovibrational cross sections and rates was found to be less than 50% at the rotational state-to-state level, except for the smaller ones and in the low energy resonance region, and less than 20% on the overall vibrational quenching rates, except for temperatures below 50 K where resonances provide a substantial contribution. Our calculated collisional state-to-state transition rate coefficients can be used in modeling interstellar non-LTE environments and our results show that they may also be obtained from the computationally less demanding CSA or VCC-IOS methods when the high accuracy achieved by CC calculations is not required. Our CC quenching rates agree with the most recent experimental data²⁸ within the error bars.

The fairly good performance of the VCC-IOS method seems surprising, since we found in calculations on the symmetric and asymmetric stretch modes of CO₂⁷ in collisions with He that the cross sections and rate coefficients from VCC-IOS calculations

differ by one to three orders of magnitude from full CC results. The disagreement was worse for the asymmetric stretch mode with frequency 2349 cm^{−1} than for the symmetric stretch mode at 1333 cm^{−1} and the cross sections were larger for the latter mode, so we concluded in Ref. 7 that the quality of VCC-IOS ameliorates with the magnitude of the cross sections and we guessed already that VCC-IOS might perform better for the bend mode at 667 cm^{−1}. Figure S8 in the supplementary material shows total quenching cross sections from CC and VCC-IOS calculations of the bend mode at collision energies 100 and 1000 cm^{−1} calculated for hypothetical frequencies in the range from 333 to 1500 cm^{−1}. This figure confirms our expectations. It shows clearly that the VCC-IOS cross sections agree fairly well with CC results up to a certain frequency, but deviate more and more for higher frequencies. For collision energy 100 cm^{−1} this critical frequency is about 850 cm^{−1}, which is higher than the frequency of 667 cm^{−1} of the bend mode. For higher collision energies the cross section is larger and the critical frequency, i.e., the energy gap between the $v = 1$ and $v = 0$ states where the VCC-IOS cross section starts deviating from the CC result, increases; at 1000 cm^{−1} it is about 1200 cm^{−1}.

We also compared our cross sections and rates for CO₂(bend)–He collisions with data from Clary *et al.*^{15,25} calculated in the 1980s with the CSA and VCC-IOS methods and a simple atom-atom model potential based on *ab initio* Hartree–Fock calculations. Their cross sections agree fairly well with ours for collision energies above 500 cm^{−1} but at lower energies the cross sections from our potential are much larger, with the difference increasing to more than two orders of magnitude at collision energies below 10 cm^{−1}. This shows that the inclusion of long range attractive dispersion interactions is crucial to obtain reliable cross sections at lower energies and rate coefficients at lower temperatures.

Finally we note that the computer programs and the knowledge about the accuracy of the approximate but computationally simpler CSA and VCC-IOS methods will also be useful to provide similar collisional data of astronomical interest for collisions of CO₂ with H₂ and for other linear molecules of which bend mode spectra have been observed and are used in modeling, such as C₂H₂ and HCN.

SUPPLEMENTARY MATERIAL

The supplementary material contains Figs. S1–S8, which are discussed in the main text. It also contains a copy of the Fortran program that calculates the CO₂–He potential for CO₂ being deformed along the bend mode normal coordinate.

ACKNOWLEDGMENTS

We thank Ewine van Dishoeck and Arthur Bosman for stimulating and useful discussions. The work is supported by The Netherlands Organisation for Scientific Research, NWO, through the Dutch Astrochemistry Network DAN-II.

AUTHOR DECLARATIONS

Conflict of Interest

The authors have no conflicts to disclose.

Author Contributions

Taha Selim: Conceptualization (supporting); Data curation (equal); Formal analysis (supporting); Investigation (equal); Methodology (supporting); Software (equal); Validation (equal); Visualization (equal); Writing – original draft (supporting). **Ad van der Avoird:** Conceptualization (equal); Data curation (supporting); Formal analysis (equal); Investigation (supporting); Methodology (supporting); Software (supporting); Supervision (equal); Validation (equal); Visualization (equal); Writing – original draft (lead). **Gerrit C. Groenenboom:** Conceptualization (equal); Data curation (equal); Formal analysis (equal); Funding acquisition (lead); Investigation (equal); Methodology (equal); Project administration (lead); Resources (lead); Software (equal); Supervision (lead); Validation (equal); Visualization (supporting); Writing – original draft (equal).

DATA AVAILABILITY

The data that support the findings of this study are available within the article and its supplementary material.

REFERENCES

- ¹E. Roueff and F. Lique, *Chem. Rev.* **113**, 8906 (2013).
- ²A. G. Palluet, F. Thibault, and F. Lique, *J. Chem. Phys.* **156**, 104303 (2022).
- ³L. Song, A. van der Avoird, and G. C. Groenenboom, *J. Phys. Chem. A* **117**, 7571 (2013).
- ⁴L. Song, N. Balakrishnan, A. van der Avoird, T. Karman, and G. C. Groenenboom, *J. Chem. Phys.* **142**, 204303 (2015).
- ⁵K. M. Walker, L. Song, B. H. Yang, G. C. Groenenboom, A. van der Avoird, N. Balakrishnan, R. C. Forrey, and P. C. Stancil, *Astrophys. J.* **811**, 27 (2015).
- ⁶L. Song, N. Balakrishnan, K. M. Walker, P. C. Stancil, W.-F. Thi, I. Kamp, A. van der Avoird, and G. C. Groenenboom, *Astrophys. J.* **813**, 96 (2015).
- ⁷T. Selim, A. Christianen, A. van der Avoird, and G. C. Groenenboom, *J. Chem. Phys.* **155**, 034105 (2021).
- ⁸T. Selim, A. van der Avoird, and G. C. Groenenboom, *J. Chem. Phys.* **157**, 064105 (2022).
- ⁹A. M. S. Boonman, E. F. van Dishoeck, F. Lahuis, S. D. Doty, C. M. Wright, and D. Rosenthal, *Astron. Astrophys.* **399**, 1047–1061 (2003).
- ¹⁰A. M. S. Boonman, E. F. van Dishoeck, F. Lahuis, and S. D. Doty, *Astron. Astrophys.* **399**, 1063–1072 (2003).
- ¹¹P. Sonnentrucker, D. A. Neufeld, P. A. Gerakines, E. A. Bergin, G. J. Melnick, W. J. Forrest, J. L. Pipher, and D. C. B. Whittet, *Astrophys. J.* **672**, 361 (2008).
- ¹²S. L. Grant *et al.*, *Astrophys. J. Lett.* **947**, L6 (2023).
- ¹³C. K. N. Patel, *Phys. Rev. A* **136**, A1187 (1964).
- ¹⁴A. A. Offenberger and D. J. Rose, *J. Appl. Phys.* **41**, 3908 (1970).
- ¹⁵D. C. Clary, *J. Chem. Phys.* **78**, 4915 (1983).
- ¹⁶W. H. Kasner and L. D. Pleasance, *Appl. Phys. Lett.* **31**, 82 (2008).
- ¹⁷D. Allen, J. Haigh, J. T. Houghton, and C. Simpson, *Nature* **281**, 660 (1979).
- ¹⁸M. López-Puertas, M. A. López-Valverde, and F. W. Taylor, *Q. J. R. Meteorol. Soc.* **118**, 499 (1992).
- ¹⁹A. G. Feofilov, A. A. Kutepov, C.-Y. She, A. K. Smith, W. D. Pesnell, and R. A. Goldberg, *Atmos. Chem. Phys.* **12**, 9013–9023 (2012).
- ²⁰JWST Transiting Exoplanet Community Early Release Science Team, *Nature* **614**, 649–652 (2023).
- ²¹T. Shimanouchi, *Tables of Molecular Vibrational Frequencies Consolidated, Volume I* (National Bureau of Standards, Gaithersburg, 1972).
- ²²D. C. Clary, *J. Chem. Phys.* **75**, 209 (1981).
- ²³D. C. Clary, *Mol. Phys.* **43**, 469 (1981).
- ²⁴D. C. Clary, *Chem. Phys.* **65**, 247 (1982).
- ²⁵A. J. Banks and D. C. Clary, *J. Chem. Phys.* **86**, 802 (1987).
- ²⁶C. T. Wickham-Jones, C. J. S. M. Simpson, and D. C. Clary, *Chem. Phys.* **117**, 9 (1987).
- ²⁷F. Lepoutre, G. Louis, and J. Taine, *J. Chem. Phys.* **70**, 2225 (1979).
- ²⁸R. M. Siddles, G. J. Wilson, and C. J. S. M. Simpson, *Chem. Phys.* **189**, 779 (1994).
- ²⁹A. D. Bosman, S. Bruderer, and E. F. van Dishoeck, *Astron. Astrophys.* **601**, A36 (2017).
- ³⁰A. D. Bosman, “Uncovering the ingredients for planet formation,” Ph.D. thesis, Leiden University, 2019.
- ³¹L. C. Biedenharn and J. D. Louck, *Angular Momentum in Quantum Physics, Encyclopedia of Mathematics Vol. 8* (Addison-Wesley, Reading, 1981).
- ³²G. Dhont, W. B. Zeimen, G. C. Groenenboom, and A. van der Avoird, *J. Chem. Phys.* **120**, 103 (2004).
- ³³MOLPRO is a package of *ab initio* programs written by H.-J. Werner and P. J. Knowles, with contributions from R. D. Amos, A. Berning, D. L. Cooper, M. J. O. Deegan, A. J. Dobbyn, F. Eckert, C. Hampel, T. Leininger, R. Lindh, A. W. Lloyd, W. Meyer, M. E. Mura, A. Nicklaß, P. Palmieri, K. Peterson, R. Pitzer, P. Pulay, G. Rauhut, M. Schütz, H. Stoll, A. J. Stone, and T. Thorsteinsson.
- ³⁴T. H. Dunning, *J. Chem. Phys.* **90**, 1007 (1989).
- ³⁵G. C. Groenenboom and N. Balakrishnan, *J. Chem. Phys.* **118**, 7380 (2003).
- ³⁶S. F. Boys and F. Bernardi, *Mol. Phys.* **19**, 553 (1970).
- ³⁷T.-S. Ho and H. Rabitz, *J. Chem. Phys.* **104**, 2584 (1996).
- ³⁸T.-S. Ho and H. Rabitz, *J. Chem. Phys.* **113**, 3960 (2000).
- ³⁹J. K. G. Watson, *Mol. Phys.* **19**, 465 (1970).
- ⁴⁰P. R. Bunker and P. Jensen, *Molecular Symmetry and Spectroscopy*, 2nd ed. (NRC Research Press, Ottawa, 1998).
- ⁴¹D. M. Brink and G. R. Satchler, *Angular Momentum*, 3rd ed. (Clarendon, Oxford, 1993).
- ⁴²M. Abramowitz and I. A. Stegun, *Handbook of Mathematical Functions* (National Bureau of Standards, Washington, DC, 1964).
- ⁴³G. Brocks, A. van der Avoird, B. T. Sutcliffe, and J. Tennyson, *Mol. Phys.* **50**, 1025 (1983).
- ⁴⁴A. van der Avoird, P. E. S. Wormer, and R. Moszynski, *Chem. Rev.* **94**, 1931 (1994).
- ⁴⁵B. R. Johnson, *J. Chem. Phys.* **69**, 4678 (1978).
- ⁴⁶B. R. Johnson, *NRCC Proc.* **5**, 86 (1979).
- ⁴⁷R. T. Pack, *J. Chem. Phys.* **60**, 633 (1974).
- ⁴⁸S. Green, *J. Chem. Phys.* **70**, 816 (1979).
- ⁴⁹Scilab Enterprises, *SCILAB: Free and Open Source software for numerical computation*.
- ⁵⁰F. L. Schöier, F. F. S. van der Tak, E. F. van Dishoeck, and J. H. Black, *Astron. Astrophys.* **432**, 369 (2005).
- ⁵¹T. G. A. Heijmen, R. Moszynski, P. E. S. Wormer, A. van der Avoird, A. D. Rudert, J. B. Halpern, J. Martin, W. B. Gao, and H. Zacharias, *J. Chem. Phys.* **111**, 2519 (1999).